ARCHIVES OF MECHANICS
Arch. Mech. **74** (6), 441–461, 2022, DOI: 10.24423/aom.4096

Peridynamic analysis of 2-dimensional deformation and fracture based on an improved technique of exerting traction on boundary surface

Z. ZHOU, M. YU, X. WANG, Z. HUANG

State Key Laboratory of Mechanics and Control of Mechanical Structures, Nanjing University of Aeronautics and Astronautics, Yudao Street 29, Nanjing, 210016, PR China, e-mails: zhouzeyuan@nuaa.edu.cn, ym0904@nuaa.edu.cn, xinfengw@nuaa.edu.cn (corresponding author), huangzx@nuaa.edu.cn

For 2-dimensional problems in peridynamics, the transfer functions of boundary traction are constructed. The peridynamic motion equation introducing the boundary traction is improved and used to solve some typical 2-dimensional deformation and fracture problems, including the uniaxial tension and pure bending of plate, and fracture of a plate with the small circular hole or central crack. The acquired numerical solutions are close to the analytical solutions of elasticity and numerical solutions given by the finite element method. The results show that the improved technique of exerting traction on a boundary surface is valid for calculating the deformation and failure of solid. It provides a new method and path for the analysis of traction boundary value problems in peridynamics.

Key words: peridynamics, peridynamic motion equation, adaptive dynamic relaxation, traction boundary conditions.

1. Introduction

Peridynamics (PD) is a new nonlocal continuum theory of mechanics [1, 2]. Its core consists in that a weighted integral of relative displacement over a spatial domain is used instead of the spatial derivative of displacement in governing equations of deformation. Peridynamics does not need the concepts of strain and stress, because it only involves relative displacement and internal long-range forces acting between each pair of particles in a horizon $H_{\boldsymbol{x}}$ [1–4]. Therefore, peridynamics can be used to conveniently and effectively analyzed deformation accompanied by evolution of discontinuities. The peridynamics was firstly advanced by Silling [1]. Since then, it has been applied to investigate various problems associated with wave, damage, fracture and impact breakage [1, 3, 5].

Traditional stress boundary conditions are not prescribed directly in peridynamics, because it is very difficult to handle the traction and constraint im-

posed on the boundary surface of a body in peridynamics [6, 7]. In order to overcome this difficulty, Silling *et al.* suggested to set a fictitious boundary layer with thickness δ in which the displacement constraints and boundary traction are specified [8–11]. Although such a treatment can obtain good results, some unphysical artifacts often appear in computation owing to the approximate feature of the fictitious boundary layer [12]. Liu and Hong found that the boundary effect became more conspicuous as the horizon increased, and the errors in calculating the equivalent Young's modulus of the boundary layer also increased [13].

Nishawala and Ostoja-Starzewski [14] used the inverse and semi-inverse methods to solve the one- and two-dimensional peristatic problems in which the traction is exerted in a striped domain closed to the boundary surface. Parks *et al.* [15] introduced "ghost" particles to calculate pairwise forces through boundaries of subdomains. Kilic and Madenci [16] pointed out that the traction or concentration forces could not be directly applied on the boundary surface since their volume integrations were zero. They need to be converted into equivalent body forces in the fictitious boundary layer. Oterkus *et al.* [17] proposed the boundary conditions could be easily enforced via a finite element model (FEM) of the subdomain containing boundaries through the merger of FEM and the peridynamic theories. Wu and Ren [18] and Wu and Hu [19] put forward an approach based on the localized convex kernel approximation constructed by the mesh-free methods to impose boundary conditions in the state-based peridynamic method. Chen *et al.* [20] completed the peridynamic analysis to the free and forced vibration of a finite bar with a specified boundary condition.

Although the fictitious boundary layer with the thickness of horizon placed outside the natural boundary surface has been commonly used in the boundary conditions of peridynamics, when using this method to prescribe traction boundary conditions, it is necessary to firstly convert the boundary traction into the body force in the fictitious boundary layer, and at making surface corrections to the material parameters in the numerical algorithm [12, 21]. Recently, Huang [6] has proposed a new PD motion equation in which the boundary traction and the displacement constraint are introduced as independent terms. The new PD motion equation has been used to analyze the tension and vibration of rod [6], but it is not applied in 2- and 3-dimensional problems due to the underdetermined transfer functions of the boundary traction. Therefore, this paper focuses on the construction of the transfer functions of the boundary traction and solves typical 2-dimensional problems.

The outline of the paper is as follows. In Section 2, the peridynamic motion equation with boundary conditions (PDB) is improved through constructing the transfer functions of the boundary traction. In Section 3, based on the

peridynamic balance equation of energy, the bond-based constitutive model is determined. The transfer functions of boundary traction are given. The damage-fracture model and the numerical algorithm are given in Sections 4 and 5, respectively. In Sections 6, 7 and 8, we use the numerical technique to solve four 2-dimensional benchmark problems. Finally, we close this paper with a summary and the comment.

2. Peridynamic motion equation with boundary traction

The peridynamic motion equation advanced by SILLING [1] is inconsistent with the stress boundary condition. In order to offset this deficiency, a new peridynamic motion equation is proposed, which reads:

$$\int\limits_{\partial\boldsymbol{\Omega}_p} [G(\boldsymbol{x},\boldsymbol{x}')\boldsymbol{p}(\boldsymbol{x}',t) + D(\boldsymbol{x},\boldsymbol{x}')\boldsymbol{y}(\boldsymbol{x}',t)]\,\mathrm{d}a(\boldsymbol{x}') + \int\limits_{H_{\boldsymbol{x}}} (\boldsymbol{T}[\boldsymbol{x},t]\langle\boldsymbol{\xi}\rangle - \boldsymbol{T}[\boldsymbol{x}',t]\langle-\boldsymbol{\xi}\rangle)\,\mathrm{d}v(\boldsymbol{x}') + \boldsymbol{f}(\boldsymbol{x},t) = \boldsymbol{\rho}(\boldsymbol{x})\dot{\boldsymbol{v}}(\boldsymbol{x},t), \tag{2.1}$$

where $\boldsymbol{\xi} = \boldsymbol{x}' - \boldsymbol{x}$, $\partial\boldsymbol{\Omega}_p$ denotes the boundary surface on which the traction $\boldsymbol{p}(\boldsymbol{x}',t)$ is prescribed and $\boldsymbol{y}(\boldsymbol{x}',t)$ is the position of the point on the boundary surface $\partial\boldsymbol{\Omega}_p$; $G(\boldsymbol{x},\boldsymbol{x}')$and $D(\boldsymbol{x},\boldsymbol{x}')$ are the transfer function of the boundary traction and of the boundary position constraint, respectively. They transfer the effects of the boundary traction and the position constraint into every particle within material. HUANG [6] has proved that Eq. (2.1) is compatible with the conservation law of momentum, when

$$\int\limits_{\boldsymbol{\Omega}} G(\boldsymbol{x},\boldsymbol{x}')\,\mathrm{d}v(\boldsymbol{x}) = 1, \tag{2.2}$$

$$\int\limits_{\boldsymbol{\Omega}} D(\boldsymbol{x},\boldsymbol{x}')\,\mathrm{d}v(\boldsymbol{x}) = 0 \tag{2.3}$$

and Eq. (2.1) is form-invariant under the Galileo transformation, if

$$\int\limits_{\partial\boldsymbol{\Omega}_p} D(\boldsymbol{x},\boldsymbol{x}')\,\mathrm{d}a(\boldsymbol{x}') = 0. \tag{2.4}$$

Meanwhile, it has been certified that the boundary traction $\boldsymbol{p}(\boldsymbol{x}',t)$, the position vectors $\boldsymbol{y}(\boldsymbol{x}',t)$ and $\boldsymbol{y}(\boldsymbol{x},t)$ must satisfy the constraints below

$$J(\boldsymbol{x},\boldsymbol{x}')[\boldsymbol{y}(\boldsymbol{x}',t) - \boldsymbol{y}(\boldsymbol{x},t)] = G(\boldsymbol{x},\boldsymbol{x}')\boldsymbol{p}(\boldsymbol{x}',t) + D(\boldsymbol{x},\boldsymbol{x}')\boldsymbol{y}(\boldsymbol{x}',t) \tag{2.5}$$

so as to make Eq. (2.1) compatible with the conservation law of angular momentum. In fact, Eq. (2.5) can be regarded as a constitutive equation with relevance to the boundary traction and position. So $J(\boldsymbol{x},\boldsymbol{x}')$ is a stiffness coefficient.

When $\boldsymbol{x}=\boldsymbol{x}'$, Eq. (2.5) reduces to

$$G(\boldsymbol{x}',\boldsymbol{x}')\boldsymbol{p}(\boldsymbol{x}',t)+D(\boldsymbol{x}',\boldsymbol{x}')\boldsymbol{y}(\boldsymbol{x}',t)=0. \tag{2.6}$$

Since $\boldsymbol{y}(\boldsymbol{x}',t)$ and $\boldsymbol{p}(\boldsymbol{x}',t)$ are correlated with each other, the constraints of $G(\boldsymbol{x}',\boldsymbol{x}')=0$ and $D(\boldsymbol{x}',\boldsymbol{x}')=0$ cannot be imposed on $G(\boldsymbol{x},\boldsymbol{x}')$ and $D(\boldsymbol{x},\boldsymbol{x}')$, which is a different argument from [6].

When the displacement boundary condition $\boldsymbol{y}(\boldsymbol{x}',t)=\bar{\boldsymbol{y}}(\boldsymbol{x}',t)=\boldsymbol{x}'+\bar{\boldsymbol{u}}(\boldsymbol{x}',t)$ is given on $\partial\boldsymbol{\Omega}$, $\partial\boldsymbol{\Omega}_p=0$. Equation (2.1) returns to the original form of the peridynamic motion equation advanced by SILLING [1], i.e.,

$$\int\limits_{H_{\boldsymbol{x}}}(\boldsymbol{T}[\boldsymbol{x},t]\langle\boldsymbol{\xi}\rangle-\boldsymbol{T}[\boldsymbol{x}',t]\langle-\boldsymbol{\xi}\rangle)\,\mathrm{d}v(\boldsymbol{x}')+\boldsymbol{f}(\boldsymbol{x},t)=\boldsymbol{\rho}(\boldsymbol{x})\dot{\boldsymbol{v}}(\boldsymbol{x},t), \tag{2.7}$$

which is the peridynamic motion equation with the displacement boundary condition.

If the stress boundary condition $\boldsymbol{p}(\boldsymbol{x}',t)=\bar{\boldsymbol{p}}(\boldsymbol{x}',t)$ is given on $\partial\boldsymbol{\Omega}_p$, then we can solve Eq. (2.5) to acquire $\boldsymbol{y}(\boldsymbol{x}',t)$, that is

$$\boldsymbol{y}(\boldsymbol{x}',t)=\frac{G(\boldsymbol{x},\boldsymbol{x}')}{J(\boldsymbol{x},\boldsymbol{x}')-D(\boldsymbol{x},\boldsymbol{x}')}\bar{\boldsymbol{p}}(\boldsymbol{x}',t)+\frac{J(\boldsymbol{x},\boldsymbol{x}')}{J(\boldsymbol{x},\boldsymbol{x}')-D(\boldsymbol{x},\boldsymbol{x}')}\boldsymbol{y}(\boldsymbol{x},t). \tag{2.8}$$

By inserting Eq. (2.8) in Eq. (2.1), the peridynamic motion equation with the stress boundary condition is given as follows:

$$\begin{aligned}\int\limits_{\partial\boldsymbol{\Omega}_p}&[\boldsymbol{\alpha}(\boldsymbol{x},\boldsymbol{x}')\bar{\boldsymbol{p}}(\boldsymbol{x}',t)+\boldsymbol{\beta}(\boldsymbol{x},\boldsymbol{x}')\boldsymbol{y}(\boldsymbol{x},t)]\,\mathrm{d}a(\boldsymbol{x}')\\&+\int\limits_{H_{\boldsymbol{x}}}(\boldsymbol{T}[\boldsymbol{x},t]\langle\boldsymbol{\xi}\rangle-\boldsymbol{T}[\boldsymbol{x}',t]\langle-\boldsymbol{\xi}\rangle)\,\mathrm{d}\nu(\boldsymbol{x}')+\boldsymbol{f}(\boldsymbol{x},t)=\boldsymbol{\rho}(\boldsymbol{x})\dot{\boldsymbol{\nu}}(\boldsymbol{x},t),\end{aligned} \tag{2.9}$$

where

$$\begin{aligned}\boldsymbol{\alpha}(\boldsymbol{x},\boldsymbol{x}')&=\frac{J(\boldsymbol{x},\boldsymbol{x}')G(\boldsymbol{x},\boldsymbol{x}')}{J(\boldsymbol{x},\boldsymbol{x}')-D(\boldsymbol{x},\boldsymbol{x}')},\\ \boldsymbol{\beta}(\boldsymbol{x},\boldsymbol{x}')&=\frac{J(\boldsymbol{x},\boldsymbol{x}')D(\boldsymbol{x},\boldsymbol{x}')}{J(\boldsymbol{x},\boldsymbol{x}')-D(\boldsymbol{x},\boldsymbol{x}')},\end{aligned} \tag{2.10}$$

which is the peridynamic motion equation with the stress boundary condition.

Let $\partial\boldsymbol{\Omega} = \partial\boldsymbol{\Omega}_{\boldsymbol{u}} \cup \partial\boldsymbol{\Omega}_p$ and $\partial\boldsymbol{\Omega}_{\boldsymbol{u}} \cap \partial\boldsymbol{\Omega}_{\boldsymbol{p}} = \emptyset$, where $\partial\boldsymbol{\Omega}_{\boldsymbol{u}}$ denotes the boundary surface subjected to the displacement constraint, while $\partial\boldsymbol{\Omega}_{\boldsymbol{p}}$ is the boundary surface prescribed by traction.

Combining Eq. (2.7) with Eq. (2.9), we have:

$$\int\limits_{\partial\boldsymbol{\Omega}_p} [\boldsymbol{\alpha}(\boldsymbol{x},\boldsymbol{x}')\bar{\boldsymbol{p}}(\boldsymbol{x}',t) + \boldsymbol{\beta}(\boldsymbol{x},\boldsymbol{x}')\boldsymbol{y}(\boldsymbol{x},t)]\,\mathrm{d}a(\boldsymbol{x}') + \int\limits_{H_{\boldsymbol{x}}} (\boldsymbol{T}[\boldsymbol{x},t]\langle\xi\rangle - \boldsymbol{T}[\boldsymbol{x}',t]\langle-\boldsymbol{\xi}\rangle)\,\mathrm{d}\nu(\boldsymbol{x}') + \boldsymbol{f}(\boldsymbol{x},t) = \boldsymbol{\rho}(\boldsymbol{x})\dot{\boldsymbol{\nu}}(\boldsymbol{x},t). \tag{2.11}$$

As a result, we acquire the peridynamic motion equation with the mixed boundary condition.

For simplicity, we further assume that

$$\frac{J(\boldsymbol{x},\boldsymbol{x}')}{J(\boldsymbol{x},\boldsymbol{x}') - D(\boldsymbol{x},\boldsymbol{x}')} = \chi \;\Leftrightarrow\; J(\boldsymbol{x},\boldsymbol{x}') = \frac{\chi}{\chi-1} D(\boldsymbol{x},\boldsymbol{x}'), \tag{2.12}$$

where $\chi = (\mathrm{V} - \mathrm{V}_B)/\mathrm{V}$, and V_B and V are the volume of a boundary layer and the volume of the body, respectively.

As a result, Eq. (2.9) and Eq. (2.11) lead to

$$\chi \int_{\partial\boldsymbol{\Omega}} [G(\boldsymbol{x},\boldsymbol{x}')\bar{\boldsymbol{p}}(\boldsymbol{x}',t)]\,\mathrm{d}a(\boldsymbol{x}') + \int\limits_{H_{\boldsymbol{x}}} (\boldsymbol{T}[\boldsymbol{x},t]\langle\xi\rangle - \boldsymbol{T}[\boldsymbol{x}',t]\langle-\xi\rangle)\,\mathrm{d}v(\boldsymbol{x}') + f(\boldsymbol{x},t) = \boldsymbol{\rho}(\boldsymbol{x})\dot{\boldsymbol{v}}(\boldsymbol{x},t), \tag{2.13}$$

$$\chi \int\limits_{\partial\boldsymbol{\Omega}_p} [G(\boldsymbol{x},\boldsymbol{x}')\bar{\boldsymbol{p}}(\boldsymbol{x}',t)]\,\mathrm{d}a(\boldsymbol{x}') + \int\limits_{H_{\boldsymbol{x}}} (\boldsymbol{T}[\boldsymbol{x},t]\langle\boldsymbol{\xi}\rangle - \boldsymbol{T}[\boldsymbol{x}',t]\langle-\boldsymbol{\xi}\rangle)\,\mathrm{d}v(\boldsymbol{x}') + f(\boldsymbol{x},t) = \boldsymbol{\rho}(\boldsymbol{x})\dot{\boldsymbol{v}}(\boldsymbol{x},t). \tag{2.14}$$

From Eq. (2.13) and Eq. (2.14), we see that the peridynamic motion equation with the traction boundary condition has the same form as that with the mixed boundary condition.

3. Peridynamic constitutive model of elastic deformation

3.1. Balance equation of energy

Let $\boldsymbol{v} = \boldsymbol{v}(\boldsymbol{x})$ be the velocity field within material. Only elastic deformation is concerned, in peridynamics, total energy conservation can be represented as

$$\frac{\mathrm{D}}{\mathrm{D}t}\int\limits_{\boldsymbol{\Omega}}\frac{1}{2}\boldsymbol{\rho}\boldsymbol{v}^2\,\mathrm{d}v+\frac{\mathrm{D}}{\mathrm{D}t}\int\limits_{\boldsymbol{\Omega}}\boldsymbol{\rho}e\,\mathrm{d}v = \int\limits_{\boldsymbol{\Omega}}\boldsymbol{v}\cdot\int\limits_{\partial\boldsymbol{\Omega}}[G(\boldsymbol{x},\boldsymbol{x}')p(\boldsymbol{x}',t)+D(\boldsymbol{x},\boldsymbol{x}')\boldsymbol{y}(\boldsymbol{x},t)]\,\mathrm{d}a(\boldsymbol{x}')\,\mathrm{d}v(\boldsymbol{x})+\int\limits_{\boldsymbol{\Omega}}\boldsymbol{f}\cdot\boldsymbol{v}\,\mathrm{d}v. \tag{3.1}$$

By Raynold's transport theorem [22], Eq. (3.1) can be rewritten as

$$\int\limits_{\boldsymbol{\Omega}}\boldsymbol{\rho}v\cdot\boldsymbol{a}\,\mathrm{d}v+\int\limits_{\boldsymbol{\Omega}}\boldsymbol{\rho}\dot{e}\,\mathrm{d}v = \int\limits_{\boldsymbol{\Omega}}\boldsymbol{v}\cdot\int\limits_{\partial\boldsymbol{\Omega}}[G(\boldsymbol{x},\boldsymbol{x}')p(\boldsymbol{x}',t)+D(\boldsymbol{x},\boldsymbol{x}')\boldsymbol{y}(\boldsymbol{x},t)]\,\mathrm{d}a(\boldsymbol{x}')\,\mathrm{d}v(\boldsymbol{x})+\int\limits_{\boldsymbol{\Omega}}\boldsymbol{f}\cdot\boldsymbol{v}\,\mathrm{d}v. \tag{3.2}$$

In terms of Eq. (2.1), Eq. (3.2) reduces to

$$\int\limits_{\boldsymbol{\Omega}}\boldsymbol{\rho}\dot{e}\,\mathrm{d}v=\int\limits_{\boldsymbol{\Omega}}\boldsymbol{v}\cdot\int\limits_{H_{\boldsymbol{x}}}(\boldsymbol{T}[\boldsymbol{x}',t]\langle-\boldsymbol{\xi}\rangle-\boldsymbol{T}[\boldsymbol{x},t]\langle\boldsymbol{\xi}\rangle)\,\mathrm{d}v(\boldsymbol{x}')\,\mathrm{d}v(\boldsymbol{x}). \tag{3.3}$$

Since $\mathrm{H}_{\boldsymbol{x}}\subset\boldsymbol{\Omega}$ is a compact supported set of $T[\boldsymbol{x}',t]\langle-\boldsymbol{\xi}\rangle$ and $T[\boldsymbol{x},t]\langle\xi\rangle$, Eq. (2.13) can be written as

$$\int\limits_{\boldsymbol{\Omega}}\boldsymbol{\rho}\dot{e}\,\mathrm{d}v=\int\limits_{\boldsymbol{\Omega}}\boldsymbol{v}\cdot\int\limits_{\boldsymbol{\Omega}}(\boldsymbol{T}[\boldsymbol{x}',t]\langle-\boldsymbol{\xi}\rangle-\boldsymbol{T}[\boldsymbol{x},t]\langle\boldsymbol{\xi}\rangle)\,\mathrm{d}v(\boldsymbol{x}')\,\mathrm{d}v(\boldsymbol{x}). \tag{3.4}$$

Interchanging $\boldsymbol{x}'$ and $\boldsymbol{x}$, and then using definition of the compact supported set, we have

$$\int\limits_{\boldsymbol{\Omega}}\boldsymbol{\rho}\dot{e}\,\mathrm{d}v=\int\limits_{\boldsymbol{\Omega}}\boldsymbol{v}\cdot\int\limits_{H_{\boldsymbol{x}}}\boldsymbol{T}[\boldsymbol{x},t]\langle\boldsymbol{\xi}\rangle[\boldsymbol{v}(\boldsymbol{x}')-\boldsymbol{v}(\boldsymbol{x})]\,\mathrm{d}v(\boldsymbol{x}')\,\mathrm{d}\boldsymbol{v}(\boldsymbol{x}). \tag{3.5}$$

By the localized hypothesis, the balance equation of energy is given as follows

$$\boldsymbol{\rho}\dot{e}=\int\limits_{H_{\boldsymbol{x}}}\boldsymbol{T}[\boldsymbol{x},t]\langle\boldsymbol{\xi}\rangle[\boldsymbol{v}(\boldsymbol{x}')-\boldsymbol{v}(\boldsymbol{x})]\,\mathrm{d}\boldsymbol{v}(\boldsymbol{x}'), \tag{3.6}$$

which has the same form as that in peridynamics without boundary conditions, and it is a base to determine the peridynamic constitutive models of hyperelastic material. Therefore, hyperelastic constitutive models in the peridynamics without boundary conditions can be inherited without modification by the peridynamics with boundary conditions.

3.2. Bond-based constitutive equation

The bond-based constitutive models have been established by SILLING (BPD) [1]. Among them, prototype microelastic model constitutive equations for elastic deformation of isotropic materials are written as [12]:

$$\boldsymbol{T}[\boldsymbol{x},t]\langle\boldsymbol{\xi}\rangle - \boldsymbol{T}[\boldsymbol{x}',t]\langle-\boldsymbol{\xi}\rangle = \frac{f(d)}{|\boldsymbol{y}(\boldsymbol{x}',t)-\boldsymbol{y}(\boldsymbol{x},t)|}[\boldsymbol{y}(\boldsymbol{x}',t)-\boldsymbol{y}(\boldsymbol{x},t)], \tag{3.7}$$

where

$$f(d) = \begin{cases} C(|\boldsymbol{\xi}|)d, & |\boldsymbol{\xi}| \le \boldsymbol{\delta}, \\ 0, & \text{otherwise}, \end{cases} \qquad d = |\boldsymbol{y}(\boldsymbol{x}',t)-\boldsymbol{y}(\boldsymbol{x},t)| - |\xi|. \tag{3.8}$$

Here, C is the so-called micromodulus, and δ is the radius of $H_{\boldsymbol{x}}$. According to the dimension of spatial configuration of a body, C takes different value, namely.

The prototype microelastic model differs from the microelastic model in the form of C. The former is written as [12]

$$C(|\boldsymbol{\xi}|) = \begin{cases} 12E/\pi\boldsymbol{\delta}^4|\boldsymbol{\xi}|, & \text{3-dimension}, \\ 12\bar{K}/\pi h\boldsymbol{\delta}^3|\boldsymbol{\xi}|, & \text{2-dimension}, \\ 3E/a\boldsymbol{\delta}^2|\boldsymbol{\xi}|, & \text{1-dimension}, \end{cases} \qquad \bar{K} = \begin{cases} 3E/4, & \text{plane stress}, \\ 9E/8, & \text{plane strain}, \end{cases} \tag{3.9}$$

In Eq. (3.9), E is Young's modulus, h is the thickness of a plate and a the cross section area of a rod. In the peridynamics without the boundary traction, Eq. (3.9) needs to be corrected in the numerical algorithm when the material points are closed to the boundary surface due to the incompleteness of the horizon [21]. However, such a correction is no longer needed in the peridynamics with the boundary traction, because the influence of the incompleteness of the horizon can be compensated by the transfer function of the boundary function.

3.3. Transfer functions of boundary constraints

The transfer functions of boundary constraints contain the transfer function of the boundary displacement constraint $D(\boldsymbol{x},\boldsymbol{x}')$ and the transfer function of the boundary traction $G(\boldsymbol{x},\boldsymbol{x}')$ [6]. They can be constructed through many ways. For example, we can choose an integrable function $q(|\boldsymbol{x}-\boldsymbol{x}'|)$ of variable to form $G(\boldsymbol{x},\boldsymbol{x}')$as follows

$$G(\boldsymbol{x},\boldsymbol{x}') = \frac{q(|\boldsymbol{x}-\boldsymbol{x}'|)}{\int_{\boldsymbol{\Omega}} q(|\boldsymbol{x}-\boldsymbol{x}'|)\,\mathrm{d}v(\boldsymbol{x})}. \tag{3.10}$$

Clearly, $G(\boldsymbol{x}, \boldsymbol{x}')$ given by Eq. (3.10) satisfy the constraints of Eqs. (2.2)–(2.4). In order to introduce as few undetermined functions as possible to represent $G(\boldsymbol{x}, \boldsymbol{x}')$, for a rectangular plate, we set:

$$q(|\boldsymbol{x}-\boldsymbol{x}'|) = \begin{cases} \left(1 - \dfrac{(|\boldsymbol{x}-\boldsymbol{x}'|)}{n\delta}\right), & \text{if } (|\boldsymbol{x}-\boldsymbol{x}'| \le \delta), \\ 0, & \text{otherwise,} \end{cases} \qquad n = \left[\frac{1}{8}\frac{LW}{S\delta}\right], \tag{3.11}$$

where L and W are the length and width of the plate, respectively. S is the total length of the boundary prescribed by non-zone traction, δ is the horizon for the material. The sign $[\bullet]$ in Eq. (3.11) represents the integer function, so n is a positive integer. Physically, the effects caused by the prescribed displacement or traction at $\boldsymbol{x}'$ on the boundary surface can be always transmitted to a point $\boldsymbol{x}$ in the interior of a body through a path, even though there is a crack or a void between the link between $\boldsymbol{x}'$ and $\boldsymbol{x}$. For simplicity, we assume that the intensity transmitted from $\boldsymbol{x}'$ to $\boldsymbol{x}$ depends only on the distance between $\boldsymbol{x}'$ and $\boldsymbol{x}$, and attenuates with the increase of the distance.

4. Peridynamic damage-fracture model

Peridynamics describes the deformation and movement through the interaction between material points. Material points are connected to each other by bonds. The bond failure between material points is introduced to describe the damage of body.

The bond stretch s is defined by [8]

$$s = \frac{|\boldsymbol{y}'-\boldsymbol{y}| - |\boldsymbol{x}'-\boldsymbol{x}|}{|\boldsymbol{x}'-\boldsymbol{x}|}. \tag{4.1}$$

Nevertheless, when the deformation stretch exceeds the critical stretch s_0, the bond between the two material points breaks irreversibly and permanently. A scalar-valued function μ is thus introduced to describe the pairwise force of a prototype microelastic brittle (PMB) material [8, 12, 21].

A scalar-valued function μ is defined as follows:

$$\mu(t, \boldsymbol{\xi}) = \begin{cases} 1, & \text{if } s(t, \boldsymbol{\xi}) < s_0, \\ 0, & \text{otherwise.} \end{cases} \tag{4.2}$$

Leading the scalar-valued function μ into Eq. (3.9), we have

$$f(d) = \begin{cases} \mu(t, \boldsymbol{\xi}) C(|\boldsymbol{\xi}|) d, & |\boldsymbol{\xi}| \le \boldsymbol{\delta}, \\ 0, & \text{otherwise,} \end{cases} \qquad d = |\boldsymbol{y}(\boldsymbol{x}', t) - \boldsymbol{y}(\boldsymbol{x}, t)| - |\boldsymbol{\xi}|. \tag{4.3}$$

Consequently, the local damage φ at a material point is introduced to illustrate the level of bond failure and is written as [8, 12, 21]:

$$\varphi(\boldsymbol{x},t) = 1 - \frac{\int_{H_{\boldsymbol{x}}} \mu(\boldsymbol{x},t,\boldsymbol{\xi})\,\mathrm{d}V_{\boldsymbol{\xi}}}{\int_{H_{\boldsymbol{x}}} \mathrm{d}V_{\boldsymbol{\xi}}}. \tag{4.4}$$

Note that the local damage ranges from 0 to 1. When $\varphi = 1$, all the interactions initially associated with the point have been eliminated, while $\varphi = 0$, means that all interactions are intact. The value of local damage represents the possibility of internal crack formation within a body [8, 12, 21].

5. Numerical solution method

The peridynamic motion equation is an integral-differential equation, the analytical solution of which is very difficult to find [23]. Consequently, the numerical techniques are usually used to solve the peridynamic motion equation [21, 23]. Firstly, a body is uniformly discretized into nodes with a certain volume in a reference configuration [8]. Unlike the finite element, all nodes form a freely deformable mesh. After discretion, the peridynamic motion equations (2.13) with the traction boundary condition can be approximately represented as

$$\chi \sum_{m=1}^{N_b} \frac{q(|\boldsymbol{x}_m - \boldsymbol{x}_i|)}{\sum_{n=1}^{N} q(|\boldsymbol{x}_m - \boldsymbol{x}_i|)V_n} \bar{\boldsymbol{p}}_m A_m + \sum_{j,N_i} C \frac{|\boldsymbol{x}_j + \boldsymbol{u}_j - \boldsymbol{x}_i - \boldsymbol{u}_i| - |\boldsymbol{x}_j - \boldsymbol{x}_i|}{|\boldsymbol{x}_j - \boldsymbol{x}_i|} \cdot \frac{\boldsymbol{x}_j + \boldsymbol{u}_j - \boldsymbol{x}_i - \boldsymbol{u}_i}{|\boldsymbol{x}_j + \boldsymbol{u}_j - \boldsymbol{x}_i - \boldsymbol{u}_i|} V_j + \boldsymbol{f}(\boldsymbol{x}_i,t) = \boldsymbol{0}_i, \tag{5.1}$$

where n is the time step number, the subscripts denote the node numbers, V_j is the volume of the node j. If the boundary condition contains the displacement constraint, it is handled in the same way as the methods proposed by SILLING [1, 2, 5, 21]. The adaptive dynamic relaxation method [21] is adopted to solve Eq. (5.1) in the following.

6. Confirmatory examples

6.1. Square plate under uniaxial tension

Consider a square plate with the side length of 50 mm, as show in Fig. 1. The mass density of material is $8000\,\mathrm{kg/m^3}$, Poisson's ratio $v = 1/3$ and Young's modulus $E = 192\,\mathrm{GPa}$. The plate is subjected to symmetrical loads of 200 MPa at the two ends in a vertical direction. The constitutive equation is given by the prototype microelastic brittle material model.

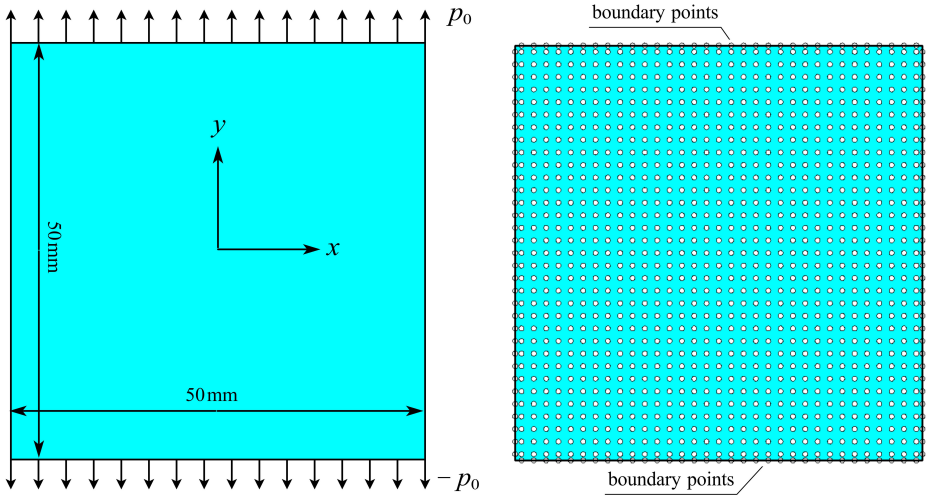

Fig. 1. Schematics of square plate under uniaxial tension and its discretization.

The square plate is discreated into a set of particles equally spaced from each other. In order to investigate the character of δ-convergence [21, 24, 25] of the improved peridynamics, four numerical examples with particle spacings of 0.02, 0.01, 0.005 and 0.0025 mm are used to demonstrate the mesh convergence. Figure 2 illustrates the computational results of the displacement at

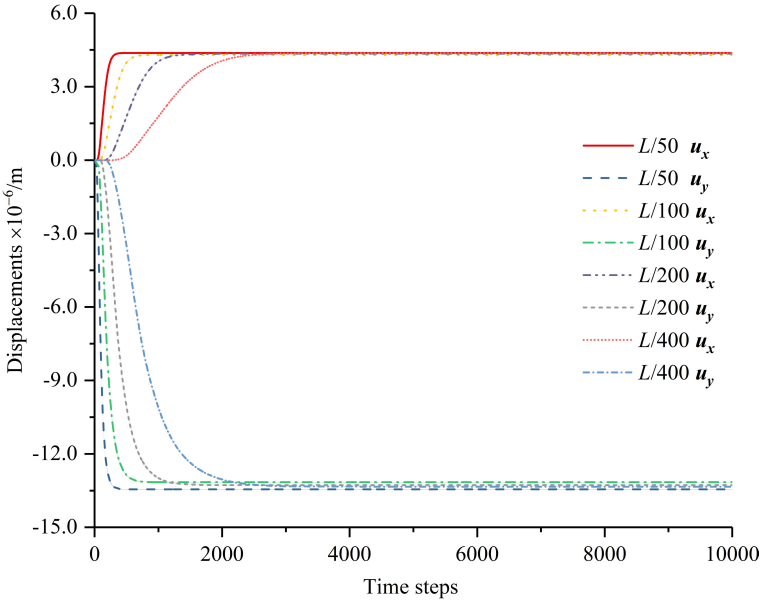

Fig. 2. Convergence of calculated results with the change of meshes and time steps.

$(-0.1225, -0.1225)$ increasing with time steps. It is easy to see that the computational results of four meshes tend to converge as the time steps reach 3000. Therefore, the time steps of 4000 are adopted in the following calculation.

In the elasticity, the displacements of the plate in Fig. 2 are analytically represented as:

$$\boldsymbol{u}_x^* = -\upsilon \frac{\boldsymbol{p}_0}{\mathrm{E}} \boldsymbol{x}, \qquad \boldsymbol{u}_y^* = \frac{\boldsymbol{p}_0}{\mathrm{E}} \boldsymbol{y}, \tag{6.1}$$

where $\boldsymbol{u}_x^*$ and $\boldsymbol{u}_y^*$ are two displacement components. Using Eq. (5.1) and Eq. (6.1), we calculate the displacements in the plate. Figure 3 shows the change of displacements at $(-0.01225, -0.01225)$ with loading. From it, we see that the results calculated by Eq. (5.1), Eq. (6.1) and BPD are very close to each other.

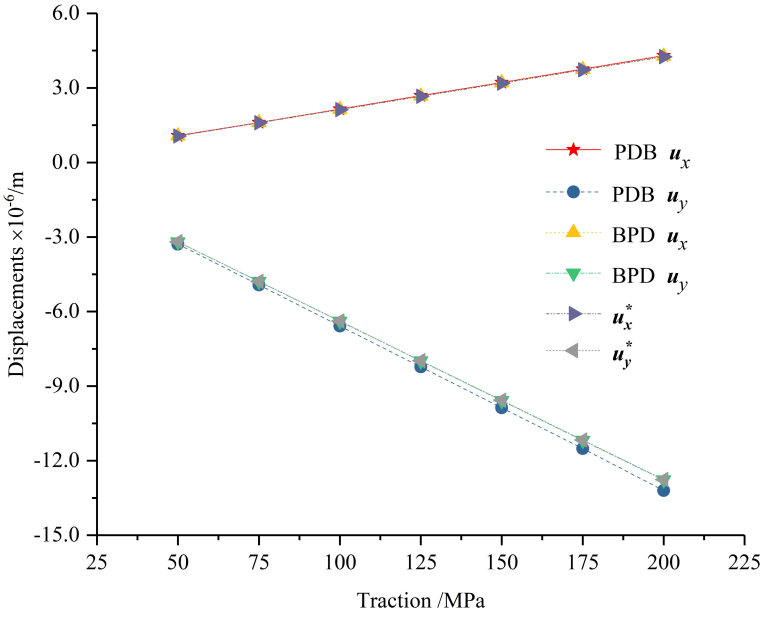

FIG. 3. Displacement components $\boldsymbol{u}_x$ and $\boldsymbol{u}_y$ at the collocation point $(-0.01225, -0.01225)$ increasing with loading.

In order to characterize the accuracy of PDB, the relative errors e_x and e_y between PDB and the elasticity are defined as

$$e_x = \left(\frac{\boldsymbol{u}_x - \boldsymbol{u}_x^*}{\boldsymbol{u}_x^*} \right), \qquad e_y = \left(\frac{\boldsymbol{u}_y - \boldsymbol{u}_y^*}{\boldsymbol{u}_y^*} \right), \tag{6.2}$$

where $\boldsymbol{u}_x$ and $\boldsymbol{u}_y$ denote the displacement components calculated by PDB.

The distribution of the relative errors given by Eq. (6.2) is illustrated in Fig. 4, which shows that the maximum relative errors occur at the corners, and other than that, the error is no more than 5% in the rest of region. Peridynamics is a nonlocal theory, different from the elasticity. Nonlocality inevitably leads to the emergence of boundary effects. Therefore, the difference between PDB and the elasticity on the boundary surface is rational in physics.

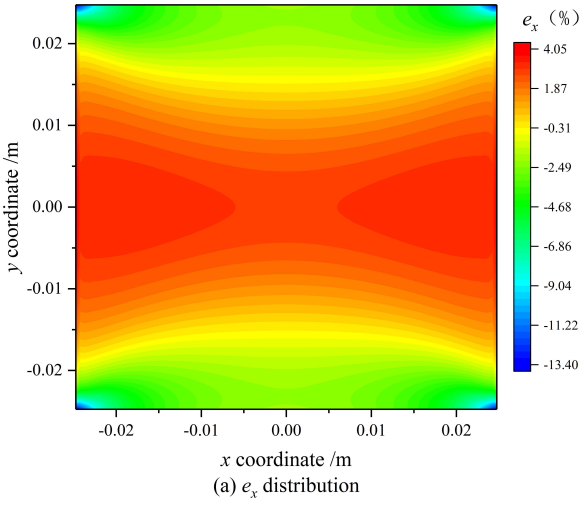

Fig. 4. Relative errors on horizontal and vertical displacement.

6.2. Bending of square plate

As a benchmark example, the uniaxial tension is the simplest case. In this section, we further examine the validity of PD under a complex loading condition

through calculating the bending of a plate. The constitutive parameters and geometrical size of the plate are the same as those in Section 6.1. The loading case and discretization scheme are illustrated in Fig. 9.

For the bending in Fig. 5, the analytical solutions (ANS) of the displacements are in the elasticity written as

$$u_x^* = -\upsilon \frac{p_0}{EL} x^2 - \frac{p_0}{EL} y^2, \qquad u_y^* = \frac{2p_0}{EL} xy. \tag{6.3}$$

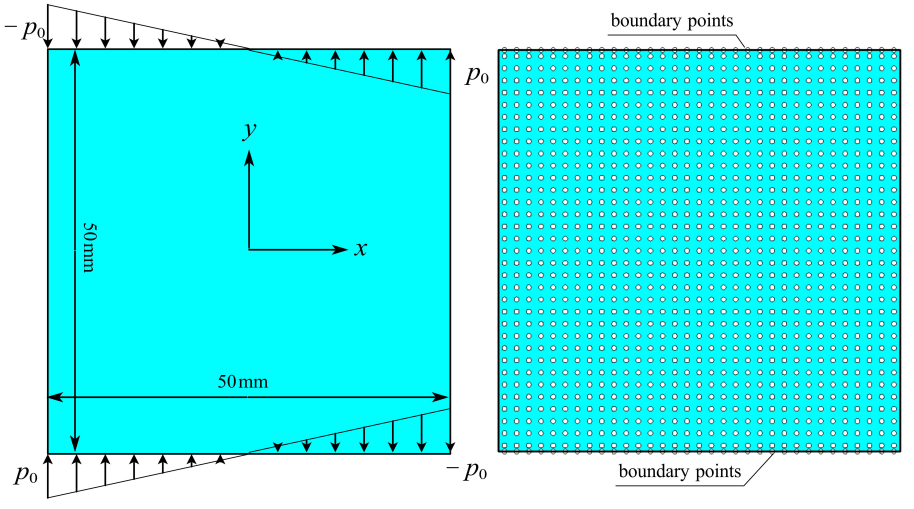

FIG. 5. Schematics of square plate under bending and its discretization.

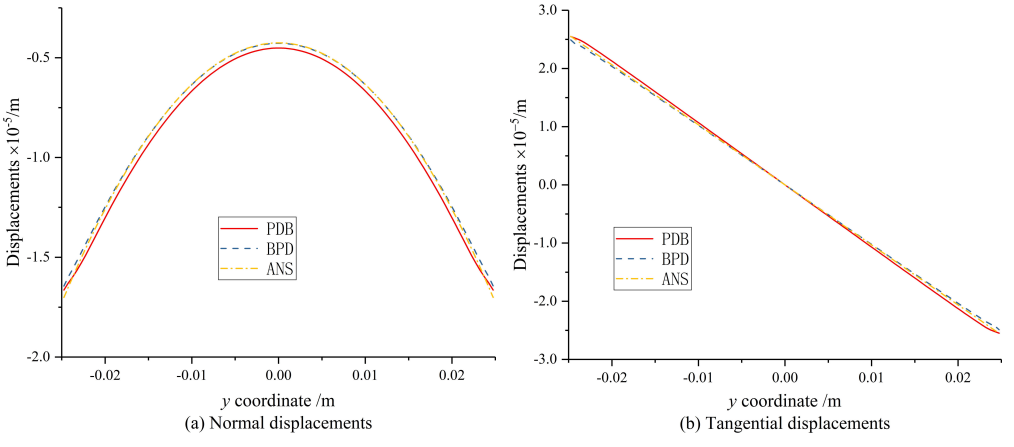

FIG. 6. The displacements on the cross-sectional surface $x = -0.02475$ given by PD and elasticity.

The displacement components on the four cross-sectional surfaces

$$x = -0.02475, \quad x = 0.01275, \quad y = -0.01275, \quad y = 0.02475$$

of the plate are shown in Figs. 6–9. We see that PDB and BPD agree well with the elasticity in the calculation of the displacements, with an error of not greater than 5%.

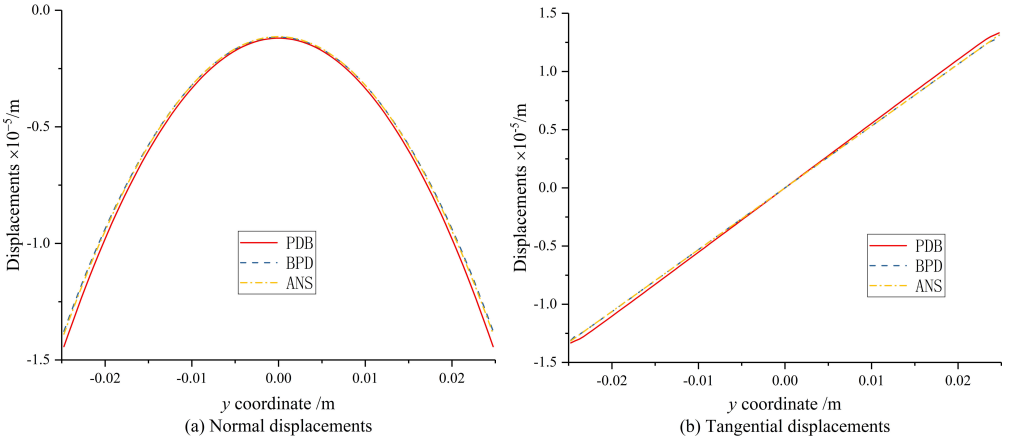

Fig. 7. The displacements on the cross-sectional surface $x = 0.01275$ given by PD and elasticity.

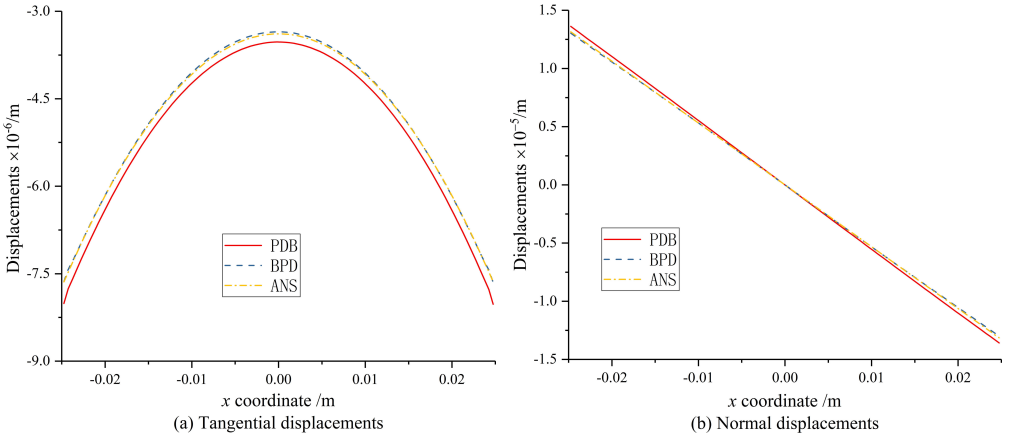

Fig. 8. The displacements on the cross-sectional surface $y = -0.01275$ given by PD and elasticity.

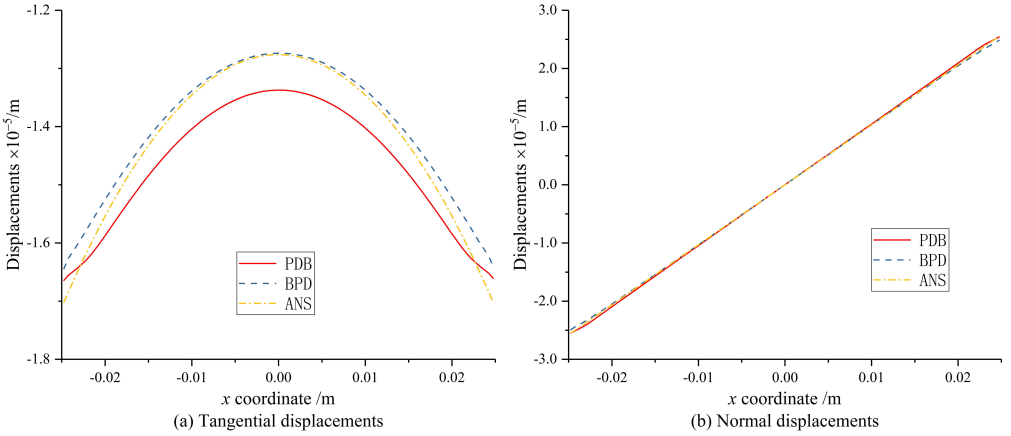

FIG. 9. The displacements on the cross-sectional surface y =0.02475 given by PD and elasticity.

7. Fracture of square plate with small circular hole under uniaxial tension

In this section, the fracture of a square plate with small circular hole under quasi-static stretching is simulated by PD. As shown in Fig. 10, The side length of the square plate is 50 mm. The circular hole with the radius of $r = 5$ mm is located at the center of the square plate. The properties of the plate are characterized by the prototype microelastic brittle model. The constitutive parameters and the discretion scheme refer to Section 6.1. The critical stretch s_0 of bond failure is taken as 0.003.

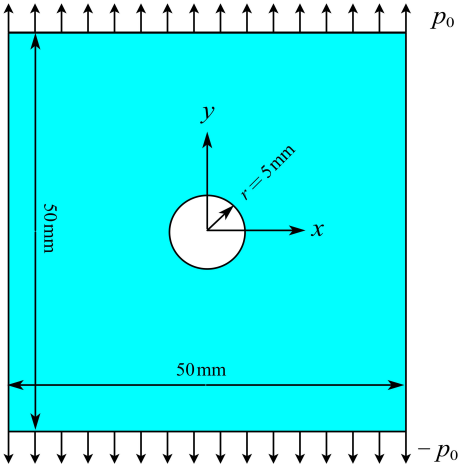

FIG. 10. Geometry of square plate with circular hole under uniaxial tension.

The tension p_0 is specified on the upper and lower side of the plate. When p_0 increases from zero to 173 MPa, the change of the relative displacement $\Delta \boldsymbol{u}$ between two midpoints of the upper and lower side with p_0 is illustrated in Fig. 11, which shows that before cracking, the relative displacement $\Delta \boldsymbol{u}$ increases linearly with the tension p_0. The prediction by PD is consistent with the result by FEM. This conclusion has been verified by many researchers [2, 17]. Moreover, the simulation from PD exhibits that the tension remains unchanged while the displacement increases sharply. This is precisely the characteristic of brittle fracture of materials under the loading control.

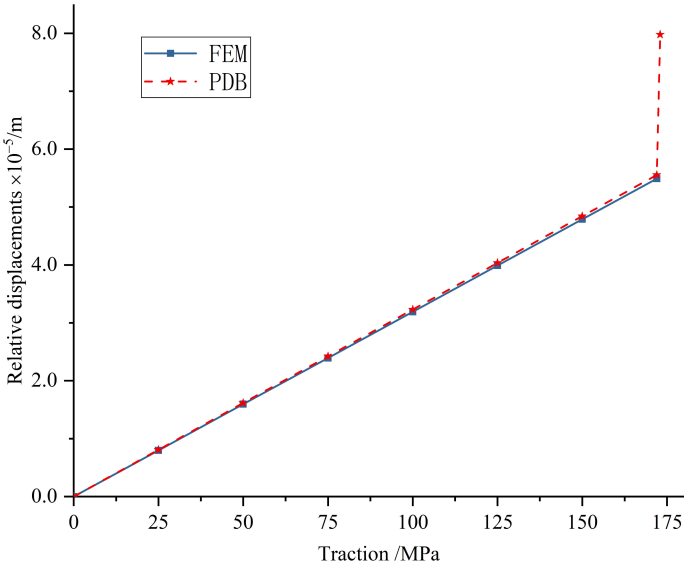

Fig. 11. Relative displacement $\Delta \boldsymbol{u}$ between two midpoints of the upper and lower side under uniaxial of two numerical simulation methods.

Figure 12 is the Moire graph to show the evolution of crack. When the time steps reach 950, two cracks initiate firstly at the stress concentration sites, and then grow symmetrically to both sides with the increase of the load. We see that, although there is no pre-existing crack in the plate, the cracks can still occur at the stress concentration sites. This is clearly an exceptional feature of the PD theory, unlike the other existing techniques that require pre-existing cracks.

At 1000 time steps, the local damage value φ caused by the cracks exceeds 0.70. Subsequently, the cracks extend rapidly in the self-similar form. Finally, when 1550 loading steps are applied, the cracks penetrate the square plate.

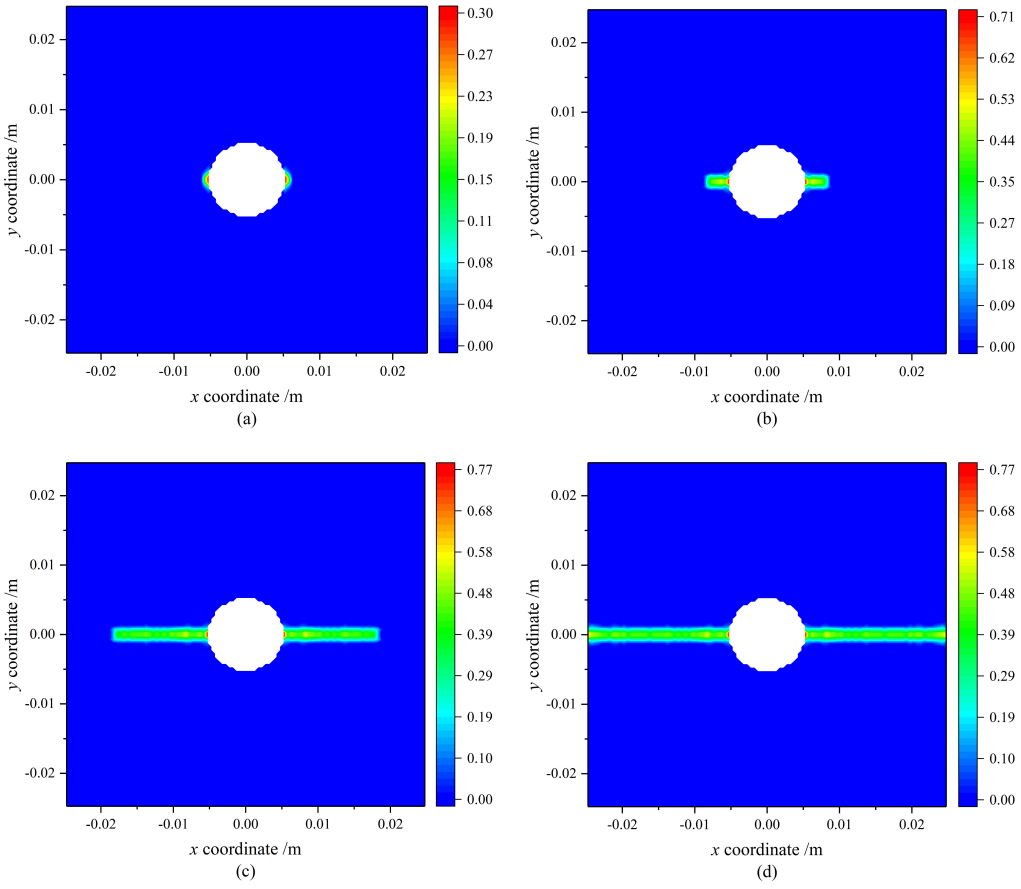

FIG. 12. Damage plots for the plate with a circular cutout at the end of (a) 950 time steps, (b) 1000 time steps, (c) 1300 time steps, and (d) 1.550 time steps.

8. Fracture of square plate with a horizonal central crack under uniaxial tension

As illustrated in Fig. 13, a square plate with the side length of 50 mm contains a central horizontal crack with the length of 10 mm. The properties of the plate are characterized by the prototype microelastic brittle model. The constitutive parameters and the discretion scheme refer to Section 6.1. The critical stretch s_0 of a bond failure is taken as 0.003, which corresponds to the critical energy release rate of $1865.7\,\mathrm{J/m^2}$.

The load for crack initiation is 145.1 MPa, while the load given by fracture mechanics [29] is 141.1 MPa, with an error not greater than 3%. After initiation, the crack extends simultaneously from two crack tips to two sides of the plate until the plate breaks. The process of the crack propagation is shown in Fig. 14a–c, which is consistent with the phenomenon observed in an experiment.

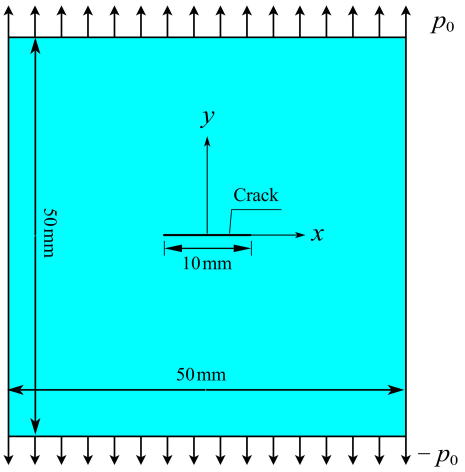

Fig. 13. Geometry of square plate with a horizontal central crack under tension.

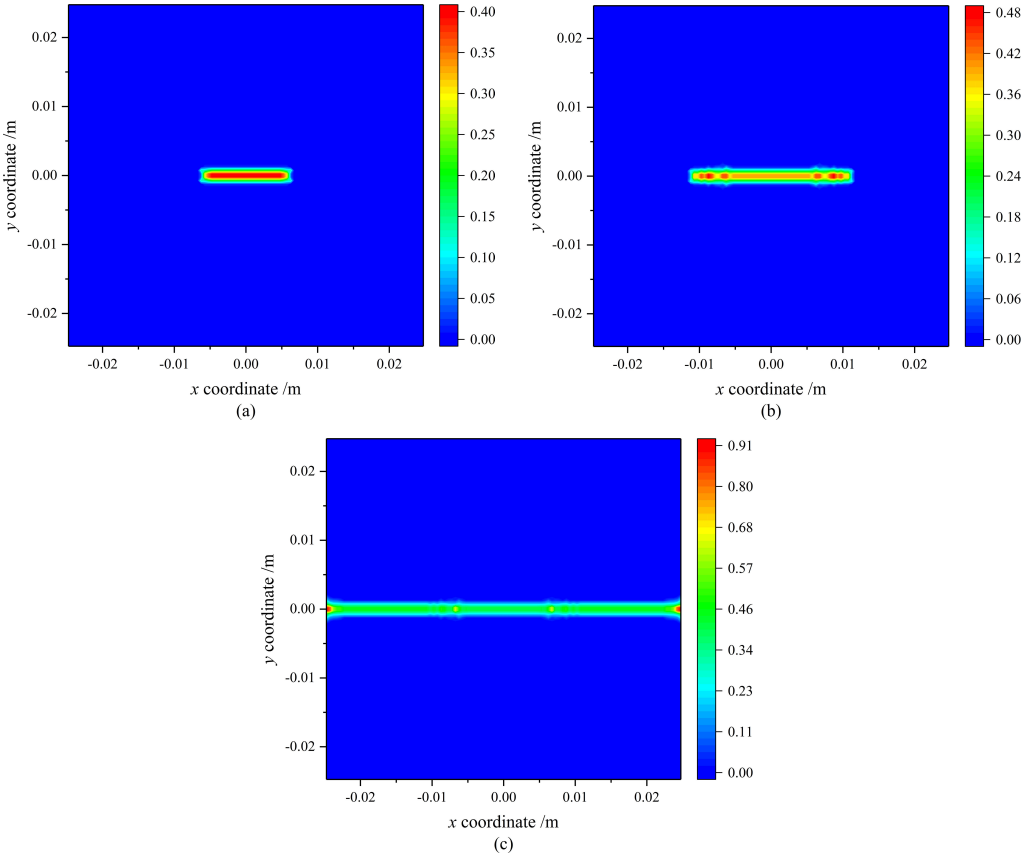

Fig. 14. Damage plots of the plate with a horizontal central crack: (a) initiation, (b) propagation, and (c) failure.

9. Conclusions

For the 2-dimensional boundary value problem of peridynamics, we construct the transfer functions of the boundary traction. Moreover, the peridynamic motion equation introducing the boundary traction is improved and is used to solve the uniaxial tension and pure bending of a square plate, the breakage of a plate with a small hole and the fracture of a plate with a horizonal central crack. The computational results are consistent with the solutions of the classical elasticity and the observed experimental phenomenon. This fact shows that the improved peridynamic motion equation is valid for calculating the deformation and failure of solid, and it provides a new method and a path for the analysis of traction boundary value problems in peridynamics.

Acknowledgements

This work has been jointly supported by the National Natural Science Foundation of China (Grant No. 12072145 and 11672129).

References

1. S.A. SILLING, *Reformulation of elasticity theory for discontinuities and long-range forces*, Journal of the Mechanics and Physics of Solids, **48**, 175–209, 2000, doi: 10.1016/s0022-5096(99)00029-0.

2. S.A. SILLING, R.B. LEHOUCQ, *Peridynamic theory of solid mechanics*, Advances in Applied Mechanics, **44**, 73–168, 2010, doi: 10.1016/S0065-2156(10)44002-8.

3. W.H. GERSTLE, *Introduction to Practical Peridynamics: Computational Solid Mechanics Without Stress and Strain*, vol. 1, World Scientific, Singapore, 2015, doi: 10.1142/9687.

4. O. WECKNER, R. ABEYARATNE, *The effect of long-range forces on the dynamics of a bar*, Journal of the Mechanics and Physics of Solids, **53**, 705–728, 2005, doi: 10.1016/j.jmps.2004.08.006.

5. S.A. SILLING, M. ZIMMERMANN, R. ABEYARATNE, *Deformation of a peridynamic bar*, Journal of Elasticity, **73**, 173–190, 2003, doi: 10.1023/B:ELAS.0000029931.03844.4f.

6. Z.X. HUANG, *Revisiting the peridynamic motion equation due to characterization of boundary conditions*, Acta Mechanica Sinica, **35**, 972–980, 2019, doi: 10.1007/s10409-019-00860-3.

7. K. ZHOU, Q. DU, *Mathematical and numerical analysis of linear peridynamic models with nonlocal boundary conditions*, SIAM Journal on Numerical Analysis, **48**, 1759–1780, 2010, doi: 10.1137/090781267.

8. S.A. SILLING, E. ASKARI, *A meshfree method based on the peridynamic model of solid mechanics*, Computers & Structures, **83**, 1526–1535, 2005, doi: 10.1016/j.compstruc.2004.11.026.

9. R.W. Macek, S.A. Silling, *Peridynamics via finite element analysis*, Finite Elements in Analysis and Design, **43**, 1169–1178, 2007, doi: 10.1016/j.finel.2007.08.012.

10. F. Bobaru, W. Hu, *The meaning, selection, and use of the peridynamic horizon and its relation to crack branching in brittle materials*, International Journal of Fracture, **176**, 215–222, 2012, doi: 10.1007/s10704-012-9725-z.

11. S.A. Silling, R.B. Lehoucq, *Convergence of peridynamics to classical elasticity theory*, Journal of Elasticity, **93**, 13–37, 2008, doi: 10.1007/s10659-008-9163-3.

12. F. Bobaru, J.T. Foster, P.H. Geubelle, S.A. Silling, *Handbook of Peridynamic Modeling*, CRC Press, Boca Raton, 2017.

13. W. Liu, J. W. Hong, *Discretized peridynamics for linear elastic solids*, Computational Mechanics, **50**, 579–590, 2012, doi: 10.1007/s00466-012-0690-1.

14. V.V. Nishawala, M. Ostoja-Starzewski, *Peristatic solutions for finite one- and two-dimensional systems*, Mathematics and Mechanics of Solids, **22**, 1639–1653, 2017, doi: 10.1177/1081286516641180.

15. M.L. Parks, R.B. Lehoucq, S.J. Plimpton, S.A. Silling, *Implementing peridynamics within a molecular dynamics code*, Computer Physics Communications, **179**, 777–783, 2008, doi: 10.1016/j.cpc.2008.06.011.

16. B. Kilic, E. Madenci, *An adaptive dynamic relaxation method for quasi-static simulations using the peridynamic theory*, Theoretical and Applied Fracture Mechanics, **53**, 194–201, 2010, doi: 10.1016/j.tafmec.2010.08.001.

17. E. Oterkus, E. Madenci, O. Weckner, S. A. Silling, P. Bogert, A. Tessler, *Combined finite element and peridynamic analyses for predicting failure in a stiffened composite curved panel with a central slot*, Composite Structures, **94**, 839–850, 2012, doi: 10.1016/j.compstruct.2011.07.019.

18. C.T. Wu, B. Ren, *Localized particle boundary condition enforcements for the state based peridynamics*, Coupled Systems Mechanics, **4**, 1–18, 2015, doi: 10.12989/csm.2015.4.1.001.

19. C.T. Wu, W. Hu, *Meshfree-enriched simplex elements with strain smoothing for the finite element analysis of compressible and nearly incompressible solids*, Computer Methods in Applied Mechanics & Engineering, **200**, 2991–3010, 2011, doi: 10.1016/j.cma.2011.06.013.

20. J.K. Chen, Y. Tian, X.Z. Cui, *Free and forced vibration analysis of peridynamic finite bar*, International Journal of Applied Mechanics, 2018, doi: 10.1142/S1758825118500035.

21. E. Madenci, E. Oterkus, *Peridynamic Theory and Its Applications*, Springer, New York, 2014.

22. G.A. Holzapfel, *Nonlinear solid mechanics: a continuum approach for engineering science*, Meccanica, **37**, 489–490, 2002. doi: 10.1023/A:1020843529530.

23. Y. Mikata, *Analytical solutions of peristatic and peridynamic problems for a 1d infinite rod*, International Journal of Solids and Structures, **49**, 2887–2897, 2012, doi: 10.1016/j.ijsolstr.2012.02.012.

24. M. H. Liu, Q. Wang, W. Lu, *Peridynamic simulation of brittle-ice crushed by a vertical structure*, International Journal of Naval Architecture and Ocean Engineering, **9**, 209–218, 2017, doi: 10.1016/j.ijnaoe.2016.10.003.

25. F. BOBARU, M. YANG, L.F. ALVES, S.A. SILLING, E. ASKARI, J. XU, *Convergence, adaptive refinement, and scaling in 1D peridynamics*, International Journal for Numerical Methods in Engineering, **77**, 852–877, 2009, doi: 10.1002/nme.2439.

26. Y.D. HA, F. BOBARU, *Studies of dynamic crack propagation and crack branching with peridynamic*, International Journal of Fracture, **162**, 229–244, 2010, doi: 10.1007/s10704-010-9442-4.

27. X.B. GU, X.P. ZHOU, X. XU, *Numerical simulation of high-speed crack propagating and branching phenomena based on peridynamics*, Applied Mathematics and Mechanics-English Edition, **37**, 729–739, 2016, doi: 10.21656/1000-0887.360310.

28. X.B. GU, X.P. ZHOU, *The numerical simulation of tensile plate with circular hole using peridynamic theory*, Chinese Journal of Solid Mechanics, **36**, 376–383, 2015 [in Chinese], doi: 10.19636/j.cnki.cjsm42-1250/o3.2015.05.002.

29. D.P. ROOKE, D.J. CARTWRIGHT, *Compendium of Stress Intensity Factors*, Her Majesty's Stationery Office, London, 1976.

Received July 04, 2022; revised version October 28, 2022.
Published online December 28, 2022.